A Comparative Study of Interface-Conforming ALE-FE scheme and Diffuse Interface AMR-LB scheme for Interfacial Dynamics

Changjuan Zhang （张昌娟）[a,b], Abbas Fakhari[c], Jie Li （李杰）[d], Li-Shi Luo（罗礼诗）[a,e,*], Tiezheng Qian （钱铁铮）[b,**]

[a]*Beijing Computational Science Research Center, Beijing 100193, China*
[b]*Department of Mathematics, Hong Kong University of Science and Technology, Clear Water Bay, Kowloon, Hong Kong*
[c]*Department of Civil & Environmental Engineering and Earth Sciences, University of Notre Dame, South Bend, IN 46556, USA*
[d]*BP Institute and Department of Engineering, University of Cambridge, Cambridge CB3 0EZ, United Kingdom*
[e]*Department of Mathematics & Statistics, Old Dominion University, Norfolk, VA 23529, USA*

Abstract

In this work, a comparative study for two simulation methods is conducted for interfacial flows in two dimensions: an arbitrary Lagrangian Eulerian (ALE) finite element method (FEM) on interface-conforming meshes and a phase field lattice Boltzmann method (LBM) on Cartesian meshes with quadtree adaptive mesh refinement (AMR). The methods are validated by simulations of a bubble without and with buoyancy force. In particular, a suspended bubble with initial nonequilibrium shape and a rising bubble driven by buoyancy force are simulated to validate the methods. Additional simulations of the breakup of a rising bubble and the bubble interaction with a horizontal wall are used to quantify the efficacy and efficiency of the two methods. It is observed that the phase field LBM is more dissipative due to the nature of the diffuse interface method used to capture the interfaces. Overall, the results obtained from both methods agree well with each other when the effects due to the numerical artifacts intrinsic to the diffuse interface method can be neglected. Also, the LBM is in general more efficient and easier to be parallelized.

*Corresponding author
**Corresponding author
Email addresses: lluo@odu.edu (Li-Shi Luo（罗礼诗）), maqian@ust.hk (Tiezheng Qian （钱铁铮）)

Keywords: adaptive mesh refinement, lattice Boltzmann method, arbitrary Lagrangian Eulerian method, finite element method, bubble dynamics, Ohnesorge number, diffuse interface modeling

1. Introduction

In the realm of fluid mechanics, dynamics of interfaces between different fluids is one of the most important and interesting subject areas, in which fascinating phenomena can be observed ubiquitously in nature or in many man-made processes, and they have been exquisitely exhibited in the experimental observations captured in Van Dyke's "Album of Fluid Motion" and [1] its modern computational reproduction, "Gallery of Fluid Motion" [2]. To this date, modeling and simulation of multiphase or multicomponent flows involving fluid-fluid interfaces remain a great challenge and a subject of much interest in computational fluid dynamics (CFD). The center piece of simulating interfacial fluid dynamics is the accurate numerical treatment of interfaces. There have been distinctive, even opposing, methodologies of treating a fluid-fluid interface, *i.e.*, interface tracking (sharp interface methods) *vs.* interface capturing (diffuse interface methods). The advocates of sharp interface methods insist that the sharp interface methodology is superior in terms of its numerical accuracy hence its fidelity to pertaining physics, while the proponents of the diffuse interface methodology promote the versatility and simplicity of the approach especially in situations involving topological changes. The arguments from both sides have merits, and techniques associated with these methodologies have made significant advances in recent decades.

This work intends to compare two entirely and drastically different methods: an interface-conforming-mesh (ICM) method and a diffuse interface (DI) method. Even though both schemes solve the incompressible Navier-Stokes equations with fluid-fluid interfaces, they are different in every aspect possible in terms of modeling philosophy and solution techniques. First of all, they treat interfaces differently: the ICM treats the fluid-fluid interfaces as discontinuities between different fluids and the interfaces obey the interface kinematic boundary conditions within the Navier-Stokes equations, while the DI method captures the interfaces with a phase field obeying the

advection-diffusion equation advected by the fluid velocity at the interfaces. Secondly, the discretization techniques used in these two methods are entirely different: the ICM method is based on the direct discretization of the Navier-Stokes equations by using the finite element method (FEM), while the diffuse interface method is based on the lattice Boltzmann equation (LBE), which is an indirect discretization of the Navier-Stokes equations based on the Boltzmann equation and kinetic theory and related to finite difference method (FDM). Thirdly, they differ in numerical mesh and data structure: the ICM method is based on the FEM on unstructured meshes with arbitrary Lagrangian Eulerian technique for mesh movement and the interfaces are a part of the mesh system, while the LBE is based on Eulerian Cartesian mesh with quadtree adaptive mesh refinement. The substantial and significant differences between these two methods make the comparative study between them challenging and yet interesting. It should also be noted that the two methods have comprised numerous advances in their respective techniques and culminated to their current state of art. Our intent is to compare the modeling fidelity and computational efficiency of these two methods.

To make this comparative study meaningful and concrete, some well-thought test cases are essential. To this end, the dynamics of a single bubble with and without buoyancy force in a rectangular container in two dimensions (2D) is chosen to conduct this study. In spite of being simple in its flow configuration and setting, the fluid dynamics of a single bubble is indeed rich and fascinating. A single bubble in a quiescent ambient liquid satisfies the Laplace law. The dynamics of a bubble driven by buoyancy force exhibits a complicated process, including acceleration process to reach a terminal velocity, and when reaching the top wall of the container, the bubble can impinge to or bounce from the wall, depending on the physical conditions in the flow. In addition, the dynamics of a bubble has been extensively studied by means of experiment [3], analysis [4], and simulation [5, 6, 7, 8, 9]. The existing data would allow us to carry out a quantitative investigation of both methods.

The remainder of the paper is organized as follows. Sec. 2 discusses the governing equations for incompressible multiphase flows and the two solution methods to be studied in this work. Specifically, Secs. 2.2 and 2.3 provide some technical details of the ALE-FEM on interface-conforming adaptive meshes and the phase field LBM on

Cartesian meshes with quadtree adaptive mesh refinement, respectively. Sec. 3 presents the numerical simulations to validate the two methods, including those of a static bubble in Sec. 3.2, a suspended bubble with initial nonequilibrium shape in Sec. 3.3, and a rising bubble driven by buoyancy force in Sec. 3.4. Sec. 4 compares the efficacy and efficiency of the two methods through simulations of the breakup of a rising bubble and the bounce of a bubble interacting with a horizontal wall, in Secs. 4.1 and 4.2, respectively. Finally, Sec. 5 concludes the paper.

2. Governing equations and simulation methods

In this section, the governing equations and two simulation methods, *i.e.*, the ALE-FEM and AMR-LBM will be presented.

2.1. Governing equations and boundary conditions

The Navier-Stokes equations for the incompressible flows of multiple immiscible Newtonian fluids are:

$$\rho\left(\frac{\partial \boldsymbol{u}}{\partial t}+\boldsymbol{u}\cdot\boldsymbol{\nabla}\boldsymbol{u}\right)=\rho\boldsymbol{g}-\boldsymbol{\nabla}p+\boldsymbol{\nabla}\cdot\mathbf{S}+\boldsymbol{T},\quad \boldsymbol{x}\in\Omega,\quad 0<t\le t_0, \tag{1a}$$

$$\boldsymbol{\nabla}\cdot\boldsymbol{u}=0, \tag{1b}$$

where $\boldsymbol{u}$ and ρ are the flow velocity and density, which is a constant in each phase or component, $\boldsymbol{g}$ is the acceleration due to an external force, p is the pressure, $\mathbf{S}:=\mu[(\boldsymbol{\nabla}\boldsymbol{u})+(\boldsymbol{\nabla}\boldsymbol{u})^{\dagger}]$ is the stress tensor, $\dagger$ denotes the transpose, μ is the dynamic viscosity, and $\boldsymbol{T}:=-\sigma(\boldsymbol{\nabla}\cdot\boldsymbol{n})\boldsymbol{n}\delta(\boldsymbol{r}-\boldsymbol{r}_{\mathrm{b}})$ is the capillary force density, σ denotes the interfacial tension, $\boldsymbol{n}$ is unit vector out-normal to the bubble interface, δ is the Dirac function, and $\boldsymbol{r}_{\mathrm{b}}$ denote the interface position.

The interface moves with the fluid velocity $\boldsymbol{u}$. As a result, the interface motion is described by the kinematic boundary condition for a point $\boldsymbol{r}_{\mathrm{b}}$ on the interface Γ:

$$\frac{\mathrm{d}\boldsymbol{r}_{\mathrm{b}}}{\mathrm{d}t}=\boldsymbol{u}(\boldsymbol{r}_{\mathrm{b}}),\quad \boldsymbol{r}_{\mathrm{b}}\in\Gamma. \tag{2}$$

The no-slip boundary condition $\boldsymbol{u}=\mathbf{0}$ is to be applied at all the boundaries. In the present study, we will take advantage of the symmetry about $x=0$ in two space dimen-

sions and carry out the computations in half space with the symmetry condition applied at $x = 0$.

2.2. Arbitrary Lagrangian Eulerian finite element method

We use the ALE-FEM [10, 11] to solve the macroscopic model described above. This method consists of an adaptive mesh technique, an arbitrary Lagrangian Eulerian method and a finite element discretization.

The interfacial motion is tracked by an adaptive mesh generator, in which the interfaces between two phases are indeed mesh lines. It is an interface-conforming method and the interface has no thickness. The vertices at an interface move with its velocity:

$$\boldsymbol{r}_{\mathrm{b}}^{n+1} = \boldsymbol{r}_{\mathrm{b}}^{n} + \boldsymbol{u}^{n}(\boldsymbol{r}_{\mathrm{b}}^{n})\Delta t, \tag{3}$$

where $\boldsymbol{r}_{\mathrm{b}}$ is the position of a vertex on the interface, $\boldsymbol{u}$ is the flow velocity, Δt is the time step, and the superscripts n and $n+1$ represent the discrete times t_n and t_{n+1} respectively. The Laplacian smoothing technique is used to relocate all other interior vertices (not at the interface), with the mesh topology being kept. Edge swapping, edge splitting and edge contraction are then adopted to maintain good mesh quality. The actual length l of an edge satisfies the condition [11]

$$r_{\min} \leq \frac{l}{l_s} \leq r_{\max}, \tag{4}$$

where l_s is a local characteristic length scale, $r_{\min}$ and $r_{\max}$ are the minimum and maximum ratios allowed. In practice, $r_{\min} = 1$ and $r_{\max} = 2.8$ work well in the present work. The characteristic length scale l_s can be controlled by controlling the number of nodes on the interface. For example, in subsection 4.2, the number of nodes on the interface is 128.

The material points on the interfaces moving with flow velocity $\boldsymbol{u}$ are conveniently described from Lagrangian point of view. For solid boundaries, Eulerian point of view from a fixed observer is more natural. The arbitrary Lagrangian Eulerian method enjoys the advantages of both Lagrangian and Eulerian methods and meanwhile alleviates the drawbacks of the two. Dynamic boundary conditions at the interfaces can be incorporated naturally and accurately in an FEM. Combining the arbitrary Lagrangian

Eulerian method with FEM, the weak form of the continuity equation and momentum equation can be discretized on a finite element triangulation. The Lagrangian technique augmented with a Uzawa method is used to enforce the divergence-free velocity exactly. The Sparse Object Oriented Linear Equations Solver (SPOOLES) is the linear solver used for the linear system generated by FEM.

2.3. Phase field lattice Boltzmann method

In this subsection we will briefly introduce the mass-conserving LBM for multiphase flows as presented by Fakhari *et al.* [12]. This method consists of a phase field LBE for tracking the interface between different fluids and a pressure-evolution LBE for recovering the hydrodynamic properties.

2.3.1. Conservative phase field lattice Boltzmann equation

The conservative phase field equation for tracking the interface between different fluids reads as

$$\frac{\partial \phi}{\partial t} + \boldsymbol{\nabla} \cdot \phi \boldsymbol{u} = \boldsymbol{\nabla} \cdot \left[M \left(\boldsymbol{\nabla} \phi - 4\phi \frac{1-\phi}{W} \boldsymbol{n} \right) \right], \tag{5}$$

where ϕ is the phase field variable such that $\phi = 0$ and $\phi = 1$ indicate the light phase and the heavy phase, respectively, and $\phi = 0.5$ indicates the nominal interface location, M is the mobility, W is the interfacial thickness, and the unit vector out-normal to the interface is computed as the following: $\boldsymbol{n} = \boldsymbol{\nabla}\phi / |\boldsymbol{\nabla}\phi|$.

Consider an interface Γ. The phase field at thermodynamic equilibrium assumes a hyperbolic tangent profile

$$\phi(\boldsymbol{r}) = \frac{1}{2} - \frac{1}{2} \tanh \left[2 \frac{d_e(\boldsymbol{r}, \Gamma)}{W} \right], \tag{6}$$

where $d_e(\boldsymbol{r}, \Gamma)$ is the *signed* distance function measured with respect to the interface Γ.

Equation (5) will be solved using the following LBE [12]:

$$\frac{\partial h_\alpha}{\partial t} + \boldsymbol{e}_\alpha \cdot \boldsymbol{\nabla} h_\alpha = -\frac{h_\alpha - h_\alpha^{eq}}{\lambda_\phi}, \tag{7}$$

where h_α is the phase field distribution function, λ_ϕ is the phase field relaxation parameter, and $\boldsymbol{e}_\alpha$ ($\alpha = 0, 1, 2, ..., 8$) is the mesoscopic velocity set. In the present work we use

the nine-velocity lattice in two space dimensions (D2Q9) [13]. The equilibrium phase field distribution function is

$$h_\alpha^{eq} = \phi\Gamma_\alpha + Mw_\alpha \frac{4\phi(1-\phi)}{Wc_s^2}\boldsymbol{e}_\alpha \cdot \boldsymbol{n}, \tag{8}$$

in which

$$\Gamma_\alpha = w_\alpha\left[1 + \frac{(\boldsymbol{e}_\alpha \cdot \boldsymbol{u})}{c_s^2} + \frac{(\boldsymbol{e}_\alpha \cdot \boldsymbol{u})^2}{2c_s^4} - \frac{(\boldsymbol{u}\cdot\boldsymbol{u})}{2c_s^2}\right], \tag{9}$$

where $c_s = c/\sqrt{3}$ is the lattice speed of sound in the system, $c = \delta x/\delta t$ is the lattice speed with δx being the lattice length scale and δt being the lattice time scale, and w_α is the weight coefficient set corresponding to the velocity set $\boldsymbol{e}_\alpha$. The numerical unit normal vector is given by $\boldsymbol{n} = \nabla\phi/|\nabla\phi + 10^{-32}|$, in which $\nabla\phi$ is calculated using isotropic finite difference. The mobility is related to the relaxation time by

$$M = \lambda_\phi c_s^2. \tag{10}$$

The phase field LBE (7) can be split into the collision and advection steps:

$$\text{collision:} \qquad \hat{h}_\alpha = h_\alpha - \frac{h_\alpha - h_\alpha^{eq}}{\lambda_\phi/\delta t + 0.5}, \tag{11a}$$

$$\text{advection:} \qquad \frac{\partial \hat{h}_\alpha}{\partial t} + \boldsymbol{e}_\alpha \cdot \boldsymbol{\nabla}\hat{h}_\alpha = 0. \tag{11b}$$

The advection step is solved using the Lax-Wendroff scheme [12]. The phase field is then calculated by taking the zeroth moment of the phase field distribution function

$$\phi = \sum_{\alpha=0}^{8} h_\alpha, \tag{12}$$

and the density ρ is updated by a linear interpolation

$$\rho = \rho_\mathrm{G} + (\rho_\mathrm{L} - \rho_\mathrm{G})\phi, \tag{13}$$

where ρ_G and ρ_L are the gas and liquid densities, respectively.

2.3.2. Pressure-evolution lattice Boltzmann equation

In order to recover the Navier-Stokes equations (1), the following LBE is used [12]

$$\frac{\partial g_\alpha}{\partial t} + \boldsymbol{e}_\alpha \cdot \boldsymbol{\nabla} g_\alpha = -\boldsymbol{\Lambda}\left(g_\alpha - g_\alpha^{eq}\right) + G_\alpha, \tag{14}$$

in which

$$G_\alpha = (\boldsymbol{e}_\alpha - \boldsymbol{u}) \cdot \left[(\Gamma_\alpha - w_\alpha) c_s^2 \boldsymbol{\nabla} \rho + \Gamma_\alpha (\boldsymbol{F}_s + \boldsymbol{F}_b) \right] \tag{15}$$

and

$$g_\alpha^{eq} = \rho c_s^2 \Gamma_\alpha + w_\alpha (p - \rho c_s^2), \tag{16}$$

where g_α is the particle distribution function, $\boldsymbol{\Lambda}$ is the generalized collision operator, p is the pressure, $\boldsymbol{F}_b = \rho \mathbf{g}$ is the body force, and $\boldsymbol{F}_s = \mu_\phi \boldsymbol{\nabla} \phi$ is the surface tension force with the chemical potential being

$$\mu_\phi = \frac{48\sigma}{W} \phi(\phi - 1)(\phi - 0.5) - \frac{3\sigma W}{2} \nabla^2 \phi, \tag{17}$$

where σ is the surface tension.

The pressure-evolution LBE (14) can be solved in two steps:

$$\text{collision:} \qquad \hat{g}_\alpha = \bar{g}_\alpha - \mathbf{M}^{-1} \hat{\mathbf{S}} \mathbf{M} \left(\bar{g}_\alpha - \bar{g}_\alpha^{eq} \right) + \delta t \, G_\alpha^{\mathrm{MD}}, \tag{18a}$$

$$\text{advection:} \qquad \frac{\partial \hat{g}_\alpha}{\partial t} + \boldsymbol{e}_\alpha \cdot \boldsymbol{\nabla} \hat{g}_\alpha = 0, \tag{18b}$$

where $\mathbf{M}$ is the orthogonal transformation matrix, $\hat{\mathbf{S}}$ is the diagonal relaxation matrix, and the following change of variable was used to maintain an explicit scheme [14]

$$\bar{g}_\alpha = g_\alpha + \frac{1}{2} \mathbf{S} \left(g_\alpha - g_\alpha^{eq} \right) - \frac{\delta t}{2} G_\alpha, \tag{19}$$

where the modified equilibrium distribution function reads as

$$\bar{g}_\alpha^{eq} = g_\alpha^{eq} - \frac{\delta t}{2} G_\alpha^{\mathrm{CD}}. \tag{20}$$

The hydrodynamic properties are calculated by

$$\boldsymbol{u} = \frac{1}{\rho c_s^2} \sum_\alpha \bar{g}_\alpha \boldsymbol{e}_\alpha + \frac{\delta t}{2\rho} \left(\boldsymbol{F}_s^{\mathrm{CD}} + \boldsymbol{F}_b \right), \tag{21a}$$

$$p = \sum_\alpha \bar{g}_\alpha + \frac{\delta t}{2} c_s^2 \boldsymbol{u} \cdot \boldsymbol{\nabla} \rho. \tag{21b}$$

Note that the subscripts CD and MD stand for central-difference and mixed-difference stencils, respectively [14]. The implementation of the adaptive-mesh refinement (AMR) algorithm has been detailed previously, in both 2D [12] and 3D [15].

2.3.3. Boundary conditions

In the AMR-LBM simulations, we use symmetric boundary conditions at the right side of the domain. At the bottom, top, and left walls the no-slip boundary condition is realized using the mid-link bounce-back for the hydrodynamic distribution function $\hat{g}_\alpha$. The boundary condition for the phase field distribution function is also mid-link bounce-back at the bottom and left walls; however, special treatment is needed for the top wall, where the wall is super-hydrophilic (complete wetting). For a given equilibrium contact angle θ_e, the phase field variable at the wall ϕ_w can be obtained from the following relation [16]:

$$\hat{\boldsymbol{n}}_\mathrm{w} \cdot \boldsymbol{\nabla}\phi|_\mathrm{w} = -\frac{4}{W}\phi_\mathrm{w}(1-\phi_\mathrm{w})\cos\theta_e, \tag{22}$$

where $\hat{\boldsymbol{n}}_\mathrm{w}$ is the unit vector out-normal to the top wall. After finding the phase field value at the ghost cells off the top wall with $\theta_e = 0$, the anti-bounce-back boundary condition for the unknown phase field distributions is implemented according to [17]

$$\bar{h}_\beta(\boldsymbol{x}_\mathrm{s}) = -\bar{h}_\alpha(\boldsymbol{x}_\mathrm{f}) + 2w_\alpha\phi_\mathrm{w} \tag{23}$$

where β denotes the bounce-back direction such that $\boldsymbol{e}_\beta = -\boldsymbol{e}_\alpha$, and $\boldsymbol{x}_\mathrm{s}$ is the location of the ghost cells at the top wall. This boundary condition is used to prevent the formation of contact line in the present study. As the solid wall is made extremely hydrophilic, the integrity of the liquid film between the bubble and the wall can be maintained.

3. Numerical results and discussion

3.1. Control parameters

The dynamics of a bubble is controlled by seven parameters, including the liquid density ρ_L, the gas density ρ_G, the liquid viscosity μ_L, the gas viscosity μ_G, the surface tension σ, the gravitational acceleration $\mathbf{g} = (0, g)^T$, and the initial diameter of the bubble D (as a characteristic length). In all the numerical simulations presented below, the liquid density is $\rho_\mathrm{L} = 1000$ kg/m^3, the gas density is $\rho_\mathrm{G} = 1$ kg/m^3 (with a large density ratio 1000), the gas viscosity is $\mu_\mathrm{G} = 10^{-5}$ Pa·s, the gravitational acceleration is $g = -10$ m/s^2, and the diameter of the initial circular bubble is $D = 1$ mm. Note that we will specify the bubble shape and size if the initial shape is not circular.

We consider three dimensionless parameters as follows. The first dimensionless parameter is the Bond number Bo:

$$\mathrm{Bo} := \frac{\Delta\rho g D^2}{\sigma}, \tag{24}$$

where $\Delta\rho := \rho_\mathrm{L} - \rho_\mathrm{G}$ is the difference between the liquid and gas densities. The Bond number measures the gravitational force relative to the interfacial tension force. The second dimensionless parameter is the gravity Reynolds number $\mathrm{Re_g}$:

$$\mathrm{Re_g} := \frac{\rho_\mathrm{L} g^{1/2} D^{3/2}}{\mu_\mathrm{L}}, \tag{25}$$

which is the ratio of the inertial force to the viscous force. In the numerical simulations presented in what follows, both the surface tension σ and the liquid viscosity μ_L will vary, and hence the dimensionless parameters Bo and $\mathrm{Re_g}$ will vary accordingly. In addition to Bo and $\mathrm{Re_g}$, the third dimensionless parameter is the Ohnesorge number Oh:

$$\mathrm{Oh} := \frac{\mu_\mathrm{L}}{(\rho_\mathrm{L}\sigma D)^{1/2}}, \tag{26}$$

which measures the viscous force relative to the inertial and interfacial tension forces. Because of $\rho_\mathrm{L} \gg \rho_\mathrm{G}$ and $\Delta\rho \approx \rho_\mathrm{L}$, we have

$$\mathrm{Oh} \approx \sqrt{\mathrm{Bo}}/\mathrm{Re_g}.$$

The parameter Oh is to be used to analyze the damped oscillatory behaviors of the bubbles [18]. Physically, Oh can be understood as the ratio of two time scales: (i) the time scale for oscillation $\tau_\mathrm{osc} \sim \sqrt{\rho_\mathrm{L} D^3/\sigma}$ determined by the inertial and interfacial tension forces, and (ii) the time scale for velocity relaxation $\tau_\mathrm{rel} \sim \rho_\mathrm{L} D^2/\mu_\mathrm{L}$ determined by the inertial and viscous forces, with $\mathrm{Oh} = \tau_\mathrm{osc}/\tau_\mathrm{rel}$. If τ_osc is much smaller than τ_rel, then Oh is small, the viscous damping is weak, and oscillatory behaviors occur in the underdamped regime. Otherwise, the viscous damping is strong, and oscillations are suppressed in the overdamped regime.

3.2. Numerical test at equilibrium

A static bubble in liquid is used as a benchmark problem here to validate the AMR-LBM and ALE-FEM for two-phase flows in two dimensions. The computational domain in AMR-LBM simulations is $[-2.5, 0] \times [-2.5, 2.5]$ mm^2 and that in ALE-FEM

simulations is $[0, 2.5] \times [-2.5, 2.5]$ mm^2, with the symmetric boundary condition applied at $x = 0$ for both methods. The static bubble is centered at $(0, 0)$ with the radius given by $R = D/2 = 0.5$ mm. In ALE-FEM simulations, the number of interface nodes is 128. As a result, the resolution is about $\frac{1}{2}\pi D/128 : 2.5\text{mm} = \pi/640$. As to the resolution in AMR-LBM simulations, the finest grid is $1/128$ of the domain width 2.5 mm. The interfacial width W is 5 lattice units, and the mobility M is 0.03 lattice units in all the AMR-LBM simulations presented in this work. The no-slip condition is applied at all other boundaries. The surface tension is $\sigma = 0.001$ N/m and the liquid viscosity μ_{L} is varied to obtain the desired Oh. No gravitational acceleration is applied here, and the only relevant dimensionless parameter is Oh. The bubble takes the shape of

$$x^2 + y^2 - R^2 = 0, \tag{27}$$

and the phase field in AMR-LBM is initialized by

$$\phi(x, y) = \frac{1}{2} - \frac{1}{2}\tanh\left(2\frac{R - \sqrt{x^2 + y^2}}{W}\right). \tag{28}$$

The value of W is typically five times of the lattice constant of the square lattice used by the AMR-LBM. The corresponding density field is given by

$$\rho(x, y) = \frac{\rho_{\mathrm{L}} + \rho_{\mathrm{G}}}{2} - \frac{\rho_{\mathrm{L}} - \rho_{\mathrm{G}}}{2}\tanh\left(2\frac{R - \sqrt{x^2 + y^2}}{W}\right), \tag{29}$$

according to equation (13). Our numerical results are presented using dimensionless time and dimensionless velocity. For simulations without gravity, time t is rescaled by the capillary time scale

$$T_\sigma = \sqrt{\frac{\rho_{\mathrm{L}} D^3}{\sigma}}, \tag{30}$$

with the dimensionless time T given by $T = t/T_\sigma$. The accuracy of the computational methods is measured by the maximum magnitude of the spurious velocities, computed from $|\boldsymbol{u}|_{max} = (\sqrt{u^2 + v^2})_{max}$. The corresponding dimensionless velocity is the Capillary number

$$\mathrm{Ca} := \frac{\mu_{\mathrm{L}} |\boldsymbol{u}|_{max}}{\sigma}. \tag{31}$$

Figure 1 shows the results for the case with $\mu_{\mathrm{L}} = 3.1623 \times 10^{-5}$ Pa·s, *i.e.*, Oh = 0.001, for both AMR-LBM and ALE-FEM methods. Figure 1(a) illustrates the refinement mesh in AMR-LBM (left) and the body fitted unstructured mesh in ALE-FEM

(right) at the initial time instant. The left half of figure 1(b) shows the equilibrium bubble shape obtained from the AMR-LBM, together with the initial bubble shape. It is evident that they match each other accurately. The spurious velocities generated by the AMR-LBM are also displayed in the left half of figure 1(b). The magnitude of Ca defined in equation (31) is about 2.6×10^{-5}. The right half of figure 1(b) shows the equilibrium bubble shape obtained from the ALE-FEM, together with the initial one. They also match each other accurately. The magnitude of Ca generated by the ALE-FEM is about 1.8×10^{-15}, which is simply caused by the machine accuracy. Compared to the AMR-LBM, the ALE-FEM produces virtually no spurious currents. This can be attributed to the accurate force balance achieved at the interface by the ALE-FEM.

In figure 1(c), the numerical density profile from AMR-LBM and the analytic expression given by equation (29) are plotted. The density profile from ALE-FEM is also presented for comparison. It is readily seen that the numerical result is in good agreement with the analytic expression, indicating that the AMR-LBM can accurately capture the interface. The ALE-FEM is a sharp interface method by which the interface can be tracked by adapting the mesh to the interface shape. The density exhibits a sharp change across the interface.

Figure 2 shows the magnitude of Ca based on the maximum spurious currents at equilibrium and Oh in the range of $[10^{-3}, 3.5]$. The AMR-LBM always gives Ca $\sim$ 10^{-4}, which is almost independent of Oh. In the AMR-LBM simulations, the maximum spurious velocities exist in the diffuse interfacial region, as shown in figure 1(b). The ALE-FEM always gives Ca $\sim 10^{-14}$, which is due to round-off error. It is seen that the ALE-FEM results are much more accurate. We want to point out that in the ALE-FEM, finer mesh and smaller time steps are required by smaller Oh, otherwise the computation may become unstable. This is due to the weaker viscous damping at smaller Oh. In AMR-LBM simulations, the interfacial width W does not have a major effect on spurious currents, i.e., it does not change the order of magnitude of Ca.

3.3. Oscillatory behaviors of suspended bubbles

To further compare the two numerical methods, the oscillatory behaviors of suspended bubbles are studied here. In each simulation, a suspended bubble is deformed

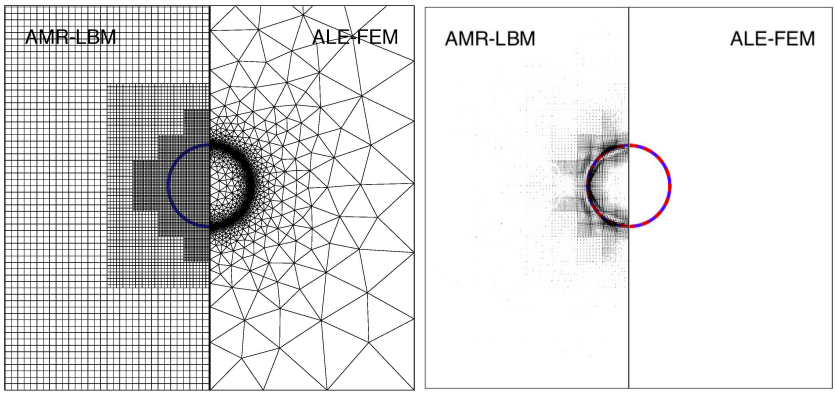

(a) (b)

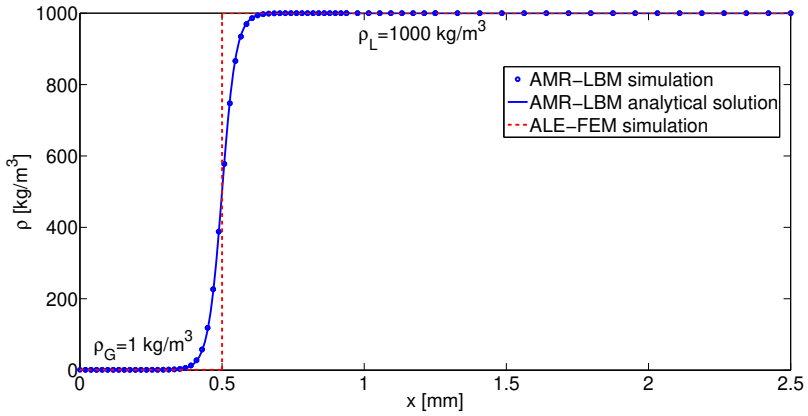

(c)

Figure 1: A static bubble in liquid. (a) Meshes used in the two methods. (b) Left: The spurious velocity distribution at equilibrium, calculated by the AMR-LBM. The blue solid line represents the initial interface and the red dashed line represents the equilibrium interface. Right: The initial bubble shape (blue solid line) and the equilibrium one (red dashed line) calculated by the ALE-FEM. (c) The density profiles across the interface, obtained from the AMR-LBM, equation (29), and the ALE-FEM.

in the beginning and gradually restore its circular shape as the system is equilibrated. Whether the bubble exhibits underdamped oscillation or not depends on the competi-
175 tion among the inertial, viscous, and capillary forces. The computational domain in AMR-LBM simulations is $[-2.5,0]\times[-2.5,2.5]$ mm^2 and that in ALE-FEM simulations is $[0,2.5]\times[-2.5,2.5]$ mm^2, with the symmetric boundary condition applied at

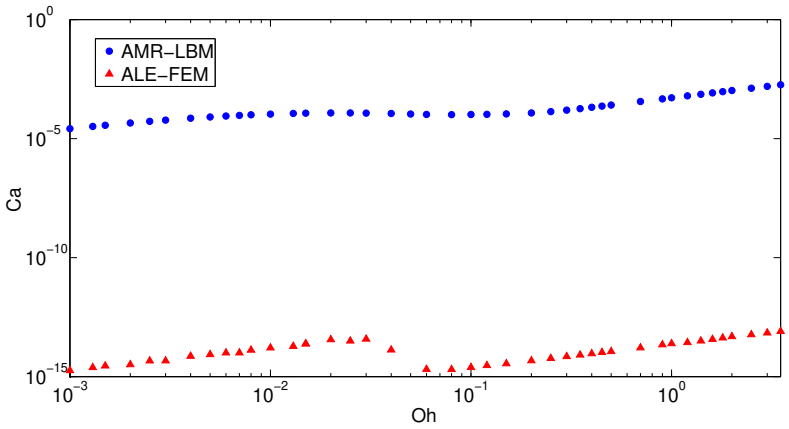

Figure 2: The magnitude of Ca based on the spurious currents at equilibrium for Oh in the range of $[10^{-3}, 3.5]$. Logarithmic scales are used for Ca and Oh.

$x = 0$ for both methods. In this subsection, the mesh resolution in ALE-FEM simulations is $\frac{1}{2}(\pi+4)/142 : 2.5 = (\pi+4)/710 \approx 1/99$, in which 142 is the number of nodes distributed at the interface. As to the mesh resolution in AMR-LBM simulations, the finest grid is 1/128 of the domain width 2.5 mm. The no-slip condition is applied at all other boundaries, same as above. No gravitational acceleration is applied here, and the only relevant dimensionless parameter is Oh, which is to be varied by varying the liquid viscosity μ_{L} or the surface tension σ.

The bubble takes the initial shape of

$$x^2 + \left(\frac{y}{3}\right)^2 = R^2, \tag{32}$$

with $R = 0.5$ mm and $(0,0)$ being the center of the elliptical bubble. To match this interface, the phase field is given by

$$\phi(x,y) = \frac{1}{2} - \frac{1}{2}\tanh\left[2\frac{d_{\mathrm{e}}(x,y)}{W}\right], \tag{33}$$

where $d_{\mathrm{e}}(x,y)$ is the signed distance function measured with respect to the ellipse $x^2 + (y/3)^2 = R^2$. As the system evolves toward the final equilibrium, the bubble may exhibit underdamped or overdamped dynamics controlled by Oh. In the dynamical regime of underdamped bubble oscillation, we intend to compare the oscillation fre-

quency and amplitude from the AMR-LBM simulations with those from the ALE-FEM simulations.

The characteristic diameter of the simulated bubble $D = \sqrt{D_x D_y} = \sqrt{3}$ mm, where $D_x = 1$ mm is the minor axis and $D_y = 3$ mm is the major axis in the beginning. The aspect ratio A_R is defined by $A_R = d_h/d_v$, where d_h is the maximum extent of the bubble in the horizontal direction and d_v is the maximum extent of the bubble in the vertical direction. In this subsection, the initial aspect ratio is $A_R = 1/3$ in all the simulations.

As stated above, the liquid density $\rho_{\mathrm{L}} = 1000\ \mathrm{kg/m^3}$, the gas density $\rho_{\mathrm{G}} = 1\ \mathrm{kg/m^3}$, and the gas viscosity $\mu_{\mathrm{G}} = 10^{-5}$ Pa·s are fixed. Now we use the surface tension $\sigma = 0.001$ N/m and vary the liquid viscosity μ_{L} to carry out a series of simulations for a quantitative study of the oscillatory behaviors of suspended bubbles. The Oh is varied by varying the liquid viscosity. In figure 3, the time evolution of the aspect ratio is plotted for different values of Oh. The results from both ALE-FEM and AMR-LBM are presented for comparison. The solid lines represent the results from ALE-FEM and the dashed lines represent the results from AMR-LBM. It is readily seen that the simulation results from AMR-LBM are in quantitative agreement with those from ALE-FEM. The two red lines (solid and dashed) are for the underdamped oscillations with the highest frequencies. As μ_{L} increases, the dimensionless parameter Oh increases as well. As a result, the bubble dynamics becomes more damped, as seen from the reduced oscillation amplitude and frequency. When Oh is large enough, the underdamped oscillation is suppressed and the bubble dynamics becomes overdamped.

Next we use the liquid viscosity $\mu_{\mathrm{L}} = 0.001$ Pa·s and vary the surface tension σ to carry out a series of simulations for further study of the oscillatory behaviors of suspended bubbles. The Oh is varied by varying the surface tension. In figure 4, the time evolution of the aspect ratio is plotted for different values of Oh. The results from both ALE-FEM and AMR-LBM are presented for comparison. The solid lines represent the results from ALE-FEM and the dashed lines represent the results from AMR-LBM. The two methods show good agreement for small Oh in the underdamped regime and large Oh in the overdamped regime. As the value of σ decreases, the dimensionless parameter Oh increases and the damping effect becomes stronger. This leads to the reduced oscillation amplitude and frequency in the underdamped regime

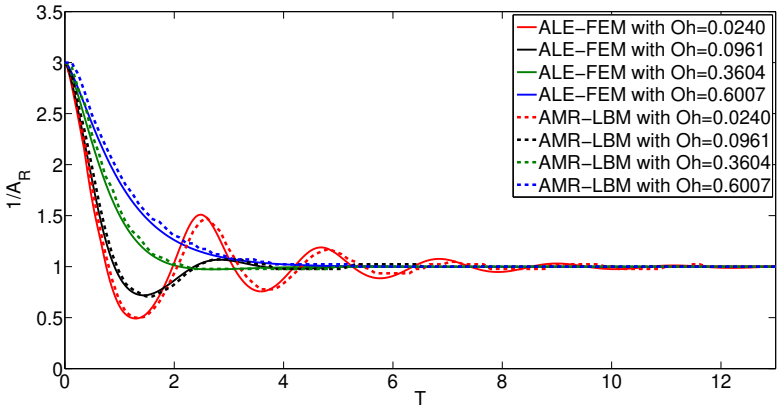

Figure 3: Time evolution of the aspect ratio A_R for different values of the liquid viscosity μ_{L}, with the surface tension $\sigma = 0.001$ N/m. The Oh is varied by varying μ_{L}. Here Oh = 0.0240, 0.0961, 0.3604, 0.6007 correspond to $\mu_{\mathrm{L}} = 0.001,\ 0.004,\ 0.015,\ 0.025$ Pa·s, respectively. The solid lines represent the results from ALE-FEM and the dashed lines represent the results from AMR-LBM, with the same color used for the same Oh. Here the dimensionless time $T = t/T_\sigma$ is measured by the capillary time scale $T_\sigma = \sqrt{\rho_{\mathrm{L}} D^3/\sigma}$.

and eventually bring the system to the overdamped regime.

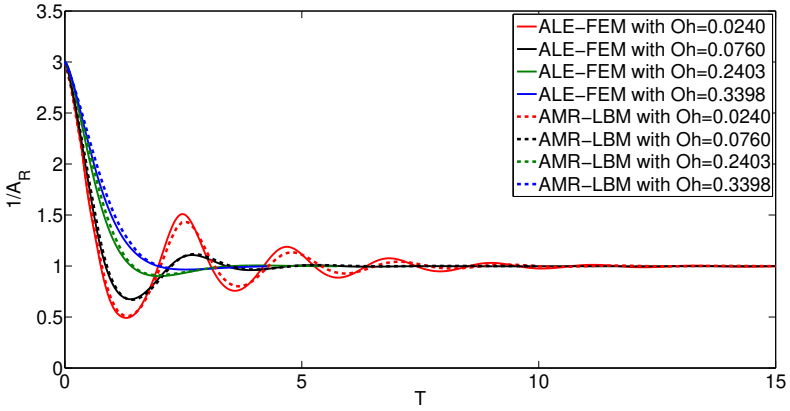

Figure 4: Time evolution of the aspect ratio A_R for different values of the surface tension σ, with the liquid viscosity $\mu_{\mathrm{L}} = 0.001$ Pa·s. The Oh is varied by varying σ. Here Oh = 0.024, 0.076, 0.2403, 0.3398 correspond to $\sigma = 10^{-3},\ 10^{-4},\ 10^{-5},\ 5\times10^{-6}$ N/m, respectively. The solid lines represent the results from ALE-FEM and the dashed lines represent the results from AMR-LBM, with the same color used for the same Oh. Here the dimensionless time $T = t/T_\sigma$ is measured by the capillary time scale $T_\sigma = \sqrt{\rho_{\mathrm{L}} D^3/\sigma}$.

To further illustrate the underdamped oscillation, figure 5 shows a series of snapshots of an oscillating bubble simulated by the AMR-LBM and ALE-FEM with μ_L = 0.001 Pa·s and $\sigma = 0.001$ N/m, which correspond to the red lines in figure 3 and figure 4 for Oh= 0.024. It is observed from figure 5 that the bubble starts from a prolate shape ($A_R < 1$) and evolves into an oblate one ($A_R > 1$) in the first row, and then evolves into a prolate one again. After several cycles, the bubble reaches the circular equilibrium shape ($A_R = 1$).

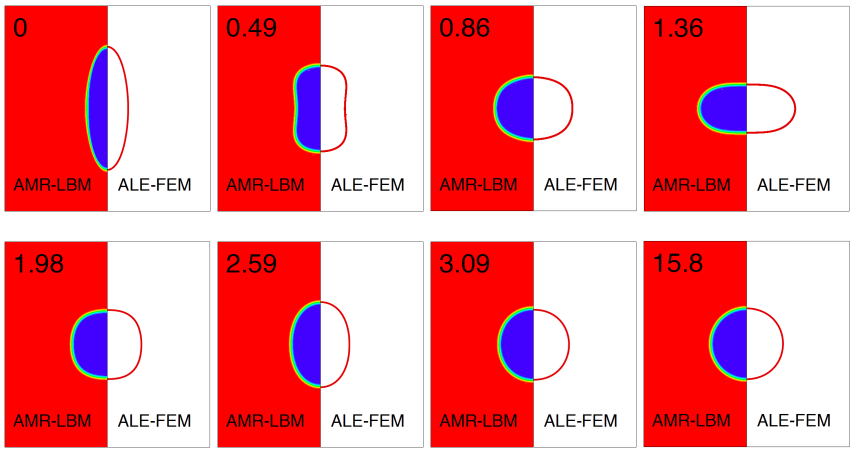

Figure 5: Time evolution of the shape of an underdamped bubble, with comparison made at the same time, with μ_L = 0.001 Pa·s and σ = 0.001 N/m. The number at the upper left corner indicates the corresponding dimensionless time T. Here the left half of each snapshot is the AMR-LBM result and the right half is the ALE-FEM result. The parameters used here correspond to those for the red curve in figure 4.

3.4. Oscillatory behaviors of rising bubbles

In this subsection, we investigate the dynamics of rising bubbles in the presence of gravitational acceleration. We will focus on the quantitative effects of the two physical parameters μ_L and σ. Numerical results from the two methods will be presented and compared. The computational domain in AMR-LBM simulations is $[-2.5,0]\times[-15,0]$ mm^2 and that in ALE-FEM simulations is $[0,2.5]\times[-15,0]$ mm^2, with the symmetric boundary condition applied at $x = 0$ for both methods. The bubble takes the initial shape of a circle, with the diameter D = 1 mm and the center located at $(x,y) = (0,-13.75)$.

Below we will give all the material parameters as dimensional quantities. The numerical results will be presented using dimensionless quantities. For the simulations with gravity here, the physical time t is rescaled by $\sqrt{D/g}$, with the dimensionless time T^* given by $T^* = t/\sqrt{D/g}$. The physical velocity v is rescaled by $\sqrt{gD}$, with the dimensionless velocity U given by $U = v/\sqrt{gD}$.

First we fix the surface tension $\sigma = 0.002$ N/m and vary the liquid viscosity μ_L to observe its quantitative effect on a rising bubble driven by the buoyancy force. In this case, the dimensionless number Bo is fixed at 4.995. The bubble velocity, defined as the velocity of the centroid of the bubble, is plotted in figure 6(a). The solid lines represent the results from ALE-FEM and the dashed lines represent the results from AMR-LBM. For $\mu_L = 0.001$ Pa·s (with Oh= 0.0224), the red lines (solid and dashed) in figure 6(a) show that the bubble accelerates immediately after its release. The bubble velocity then oscillates around some average value (not accurately defined though) for a while. The velocity drops sharply toward zero when the bubble finally approaches the top wall. For $\mu_L = 0.0015$ Pa·s (with Oh= 0.0335), the black lines (solid and dashed) in figure 6(a) show behaviors that are similar to those for $\mu_L = 0.001$ Pa·s. Note that the oscillations are weakened by the increased liquid viscosity. For $\mu_L = 0.005$ Pa·s (with Oh= 0.1118), the blue lines (solid and dashed) in figure 6(a) show that oscillations are suppressed by the large liquid viscosity.

From the above results, it is observed that as the liquid viscosity increases, Oh increases as well, leading to stronger viscous damping and weaker oscillations (in the underdamped regime) or no oscillations at all (in the overdamped regime). More specifically, as Oh increases, the underdamped oscillations show lower frequency and smaller amplitude. For a given μ_L, *i.e.*, a given Oh, the velocities from the ALE-FEM show faster oscillation and larger amplitude compared to the velocities from the AMR-LBM. This can be attributed to the diffusive transport as an additional dissipative process that is present in the diffuse interface modeling.

Figure 6(b) shows the time evolution of the aspect ratio for different values of Oh. Results from both the AMR-LBM and ALE-FEM are presented in figure 6(b), where the line styles and colors have the same correspondence as in figure 6(a). The bubble is circular in the beginning (with $A_R = 1$). It is immediately squashed (with $A_R > 1$)

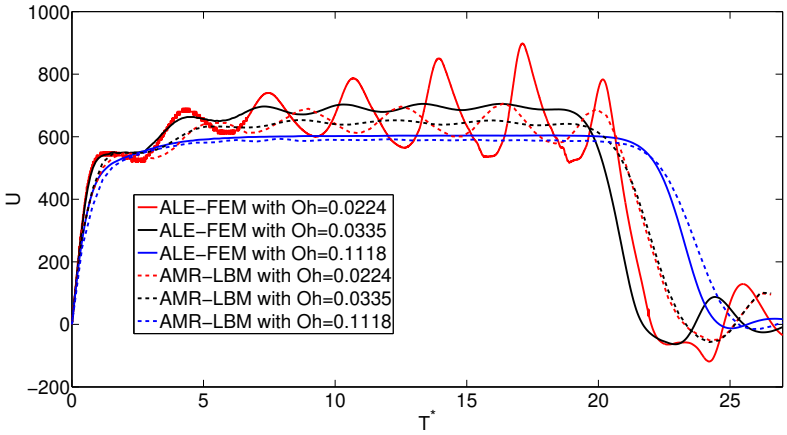

(a)

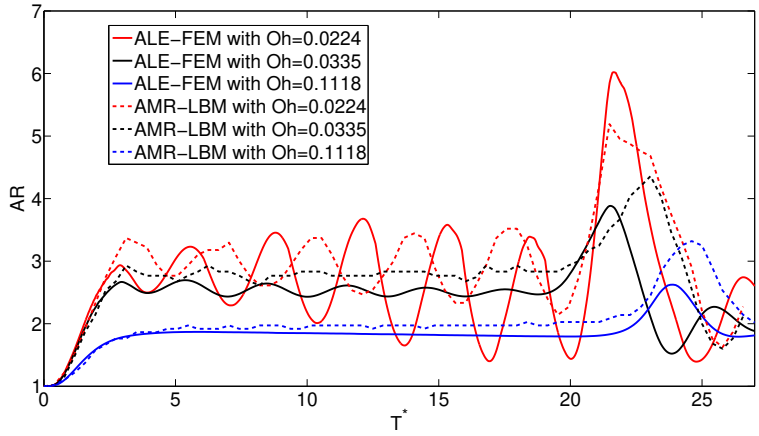

(b)

Figure 6: Comparison between the two methods, for rising bubbles with the surface tension fixed at σ = 0.002 N/m and the liquid viscosity μ_L varied. The dimensionless parameter Oh= 0.0224, 0.0335 and 0.1118 correspond to μ_L = 0.001, 0.0015 and 0.005 Pa·s, respectively. (a) Time evolution of the rising bubble's velocity for different values of μ_L. (b) Time evolution of the rising bubble's aspect ratio for different values of μ_L. The solid lines represent the results from ALE-FEM and the dashed lines represent the results from AMR-LBM, with the same color used for the same Oh.

as its rising is accelerated. In accordance with the velocity oscillations in figure 6(a), the aspect ratio displays oscillatory behaviors as well (for Oh= 0.0224 and 0.0335). As the liquid viscosity increases, the bubble deformation is reduced. This is seen from the reduced amplitude of the oscillations of A_R (from Oh= 0.0224 to 0.0335) and the nearly constant A_R during the rising process (for Oh= 0.1118). The largest Oh leads to the smallest A_R which means the smallest deformation.

Here we want to point out that the quantitative agreement between the results from the two methods is not very satisfactory. This can actually be improved by using finer mesh in AMR-LBM. In subsection 4.2, we will present more numerical results for a rising bubble in this regard.

Figure 7(a) shows the time evolution of the bubble shape for the case of small Oh= 0.0224 in figure 6(a) and figure 6(b). In this case, the aspect ratio from the ALE-FEM shows a more pronounced oscillation than that from the AMR-LBM, as seen from figure 6(b) and figure 7(a). This can be attributed to the diffusive transport as an additional dissipative process that is present in the diffuse interface modeling. Figure 7(b) shows the time evolution of the bubble shape for the case of large Oh= 0.1118 in figure 6(a) and figure 6(b). In this case, the viscous damping is strong and there is no oscillation observed for the velocity or the aspect ratio. The bubble rises with deformation in development until a stationary shape is attained. (Note that the stationary shape appears when the bubble is still far away from the top wall.)

Now we fix the liquid viscosity $\mu_{\mathrm{L}} = 0.001$ Pa·s and vary the surface tension σ to observe its quantitative effect on a rising bubble driven by the buoyancy force. In this case, the dimensionless number $\mathrm{Re_g}$ is fixed at 100. Different values of the surface tension σ (with different values of Oh) will give rise to different dynamic behaviors of the bubble. The time evolution of the bubble velocity is plotted in figure 8(a). The solid lines represent the results from ALE-FEM and the dashed lines represent the results from AMR-LBM. For $\sigma = 0.003$ N/m (with Oh= 0.0183), the red lines (solid and dashed) in figure 8(a) show that the bubble accelerates immediately after its release, as seen in all the cases. The bubble velocity shows weak oscillations around some average value (not accurately defined though) for a while. The velocity drops sharply toward zero when the bubble finally approaches the top wall. For $\sigma = 0.002$ N/m (with

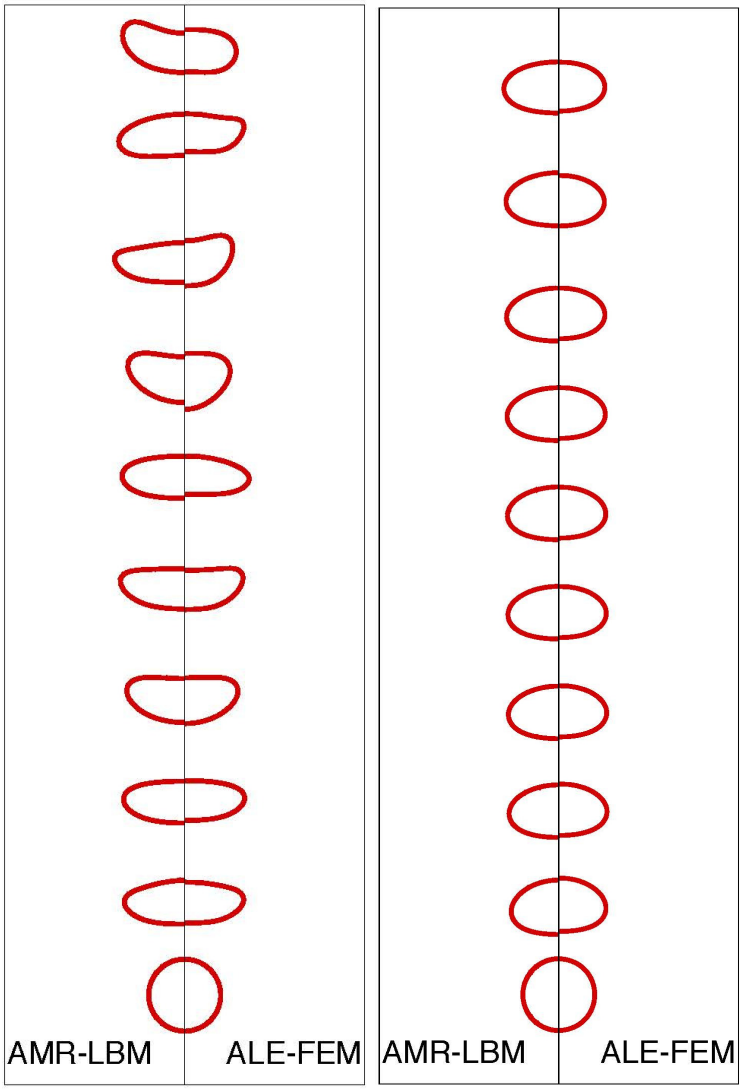

(a) (b)

Figure 7: Time evolution of the bubble shape, with comparison made at the same position, computed for σ = 0.002 N/m with Bo fixed at 4.995. (a) μ_L = 0.001 Pa·s such that Oh= 0.0224. Left: the AMR-LBM results. Right: the ALE-FEM results. (b) μ_L = 0.005 Pa·s such that Oh= 0.1118. Left: the AMR-LBM results. Right: the ALE-FEM results.

Oh= 0.0224), the black lines (solid and dashed) in figure 8(a) show strong oscillations. Compared to the case of Oh= 0.0183, the present case of Oh= 0.0224 displays larger oscillation amplitude but lower frequency. For $\sigma = 0.0002$ N/m (with Oh= 0.0707), the blue lines (solid and dashed) in figure 8(a) only show a bit oscillation in the initial stage, followed by a steady terminal velocity before the bubble approaches the top wall.

From the above results, it is observed that as the surface tension decreases, Oh increases, leading to stronger viscous damping. From $\sigma = 0.003$ N/m to $\sigma = 0.002$ N/m, the frequency of the underdamped oscillations becomes lower due to the increased viscous damping. From $\sigma = 0.002$ N/m to $\sigma = 0.0002$ N/m, the underdamped oscillations become overdamped due to the increased viscous damping. It is interesting to note that the case of $\sigma = 0.002$ N/m (with Oh= 0.0224) shows a bigger oscillation amplitude than the case of $\sigma = 0.003$ N/m (with Oh= 0.0183). Physically, a smaller surface tension leads to a larger shape deformation, and hence a slower rising velocity of the bubble. This then leads to a weaker viscous drag by the surrounding liquid, allowing a bigger oscillation amplitude to occur. For Oh= 0.0707 which is the biggest among the three cases, the shape deformation is the largest and the rising velocity is the slowest. For a given σ, *i.e.*, a given Oh, the velocities from the ALE-FEM show faster oscillation and larger amplitude compared to the velocities from the AMR-LBM. This can be attributed to the diffusive transport as an additional dissipative process that is present in the diffuse interface modeling.

Figure 8(b) shows the time evolution of the aspect ratio for different values of Oh. Results from both the AMR-LBM and ALE-FEM are presented in figure 8(b), where the line styles and colors have the same correspondence as in figure 8(a). Similar to that seen in figure 6(b), the bubble is circular in the beginning (with $A_R = 1$), and then it is immediately squashed (with $A_R > 1$) as its rising is accelerated. In accordance with the velocity oscillations in figure 8(a), the aspect ratio displays oscillatory behaviors as well (for Oh= 0.0183 and 0.0224). As the surface tension decreases, Oh increases and the viscous damping becomes relatively stronger. This leads to a lower frequency of the underdamped oscillations (if any) or no oscillations at all (in the overdamped regime). For the smallest value of σ, we have the softest bubble which exhibits the largest deformation and the slowest rising.

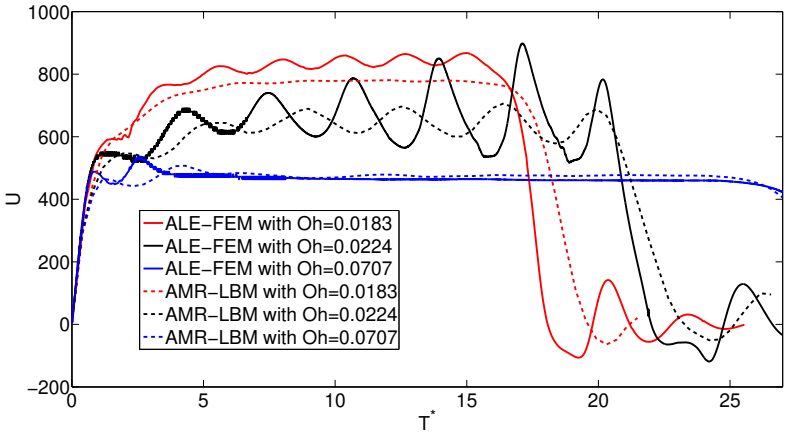

(a)

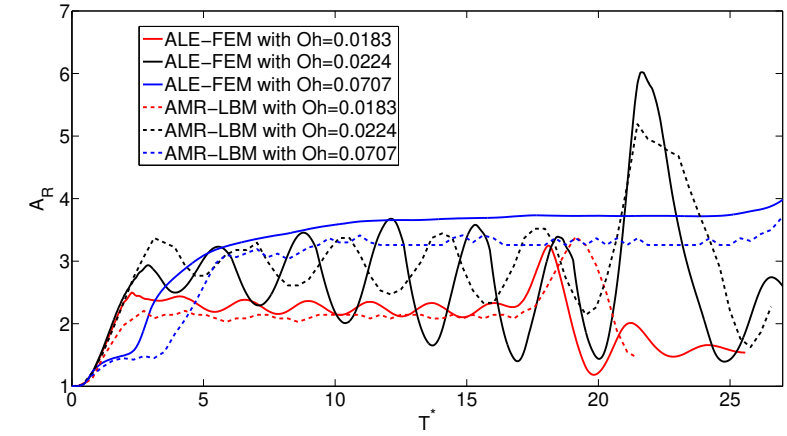

(b)

Figure 8: Comparison between the two methods, for rising bubbles with the liquid viscosity fixed at μ_L = 0.001 Pa·s and the surface tension σ varied. The dimensionless parameter Oh= 0.0183, 0.0224 and 0.0707 correspond to σ = 0.003, 0.002 and 0.0002 N/m, respectively. (a) Time evolution of the rising bubble's velocity for different values of σ. (b) Time evolution of the rising bubble's aspect ratio for different values of σ. The solid lines represent the results from ALE-FEM and the dashed lines represent the results from AMR-LBM, with the same color used for the same Oh.

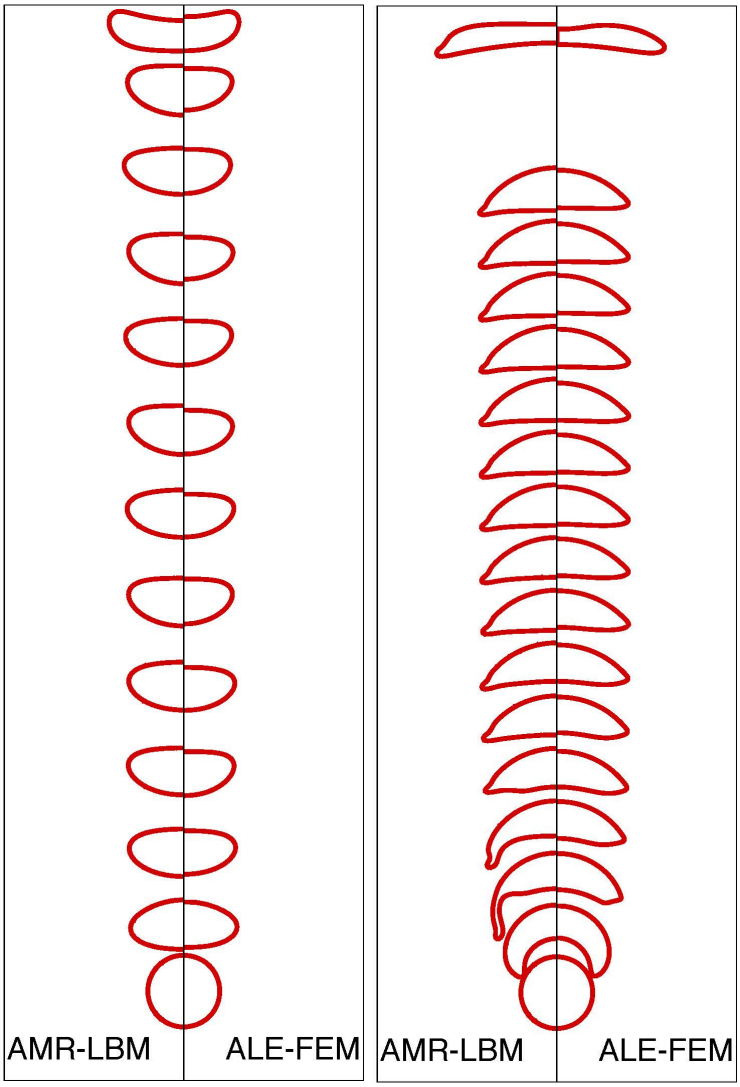

(a) (b)

Figure 9: Time evolution of the bubble shape, with comparison made at the same position, computed for μ_L = 0.001 Pa·s with Re_g fixed at 100. (a) σ = 0.003 N/m such that Oh= 0.0183. Left: the AMR-LBM results. Right: the ALE-FEM results. (b) σ = 0.0002 N/m such that Oh= 0.0707. Left: the AMR-LBM results. Right: the ALE-FEM results.

Figure 9(a) shows the time evolution of the bubble shape for the case of small Oh= 0.0183 in figure 8(a) and figure 8(b). Since the amplitude of the oscillation of A_R is small in figure 8(b), the shape oscillation of the rising bubble is not obviously seen in figure 9(a). Figure 9(b) shows the time evolution of the bubble shape for the case of large Oh= 0.0707 in figure 8(a) and figure 8(b). In this case, the dynamics is almost overdamped and the bubble eventually rises with a stable and large deformation.

The comparisons made in figures 6-9 show appreciable disparity between the AMR-LBM and ALE-FEM results. This is due to the artifact of the diffuse interface modeling used in the LBM, and this artifact can be mitigated by refining the mesh size, as shown later in Fig. 11 in subsection 4.2. Note that in figures 7 and 9, the bubble volume from AMR-LBM appears to be bigger than that from ALE-FEM. This is not a visual artifact. In fact, neither method can guarantee the volume conservation of the bubble. In AMR-LBM simulations, the volume change can be very large if the value of M is not properly chosen. In ALE-FEM simulations, the bubble volume is well conserved for large Oh, but it may change a lot for small Oh (by $\sim 5\%$ in long-term behaviors). The bubble volume becomes larger in AMR-LBM but it becomes smaller in ALE-FEM. This leads to a visible difference as seen in figures 7 and 9.

Physically, Oh is the dimensionless control parameter that distinguishes the underdamped dynamics at small Oh from the overdamped dynamics at large Oh. Here we want to point out that in all the simulations presented above, the largest Oh at which the bubble still oscillates is less than 0.1, while 0.1 is less than the smallest Oh at which the bubble no longer oscillates. Therefore, the critical value appears to be Oh $\simeq 0.1$, in semi-quantitative consistency with the results in [18], where the focus is on some different but related dynamic phenomena of rising bubbles.

Finally, we want to discuss the AMR-LBM simulations for bubbles that are very close to the top wall (in the final stage of the rising process). To maintain the integrity of the liquid film between the bubble and the top wall, the formation of the contact line is to be avoided. This is achieved by employing a solid surface that 'likes' the liquid and 'hates' the gas. In the boundary conditions we used in the AMR-LBM, the contact angle (defined on the side of liquid) is set to be 0 for the phase field ϕ.

4. Numerical capability and efficiency

In this section, we compare the two methods on their numerical capability and efficiency.

4.1. Breakup of a rising bubble

Based on the diffuse interface modeling, the AMR-LBM is capable of handling the topological changes of the interface. This makes it a versatile tool for dealing with a range of problems involving pinch-off and coalescence. The ALE-FEM is a sharp interface method, by which irregular topological changes of the interface cannot be automatically captured. Additional engineering of the mesh is needed by the ALE-FEM to deal with the topological changes, but this is not considered in the present work. Therefore, the AMR-LBM has its own advantage over the ALE-FEM when topological changes are involved, because irregular topological changes of the interface can be captured automatically.

Topological change may occur when a bubble rises in a liquid. In the test case below, the material parameters are $\mu_{\mathrm{L}} = 2 \times 10^{-4}$ Pa·s and $\sigma = 0.001$ N/m, with the dimensionless parameters Bo = 9.99, $\mathrm{Re_g}$ = 500, and Oh= 0.00633. In figure 10 we show the shape evolution for a rising bubble, obtained from the two methods. Here the comparison for bubble shape is made at the same position, with the understanding that the bubble will arrive at the same position at slightly different time instants from the two methods. In figure 10, the AMR-LBM results show that the bubble breaks up at some point during the rising process. However, the ALE-FEM results are presented up to the point immediately before the breakup. It is readily seen that before the breakup, the two methods produce bubble shapes that are close to each other, with semi-quantitative agreement.

4.2. Bounce of a rising bubble

Now we turn to a bubble interacting with a horizontal solid wall that is extremely hydrophilic. In this test, the bubble will bounce from the wall with oscillatory deformation. We carry out a simulation for $\mu_{\mathrm{L}} = 0.001$ Pa·s and $\sigma = 0.08$ N/m with Oh= 0.0035, Bo = 0.125 and $\mathrm{Re_g}$ = 100. The bubble is released with a zero initial velocity at (0 mm,

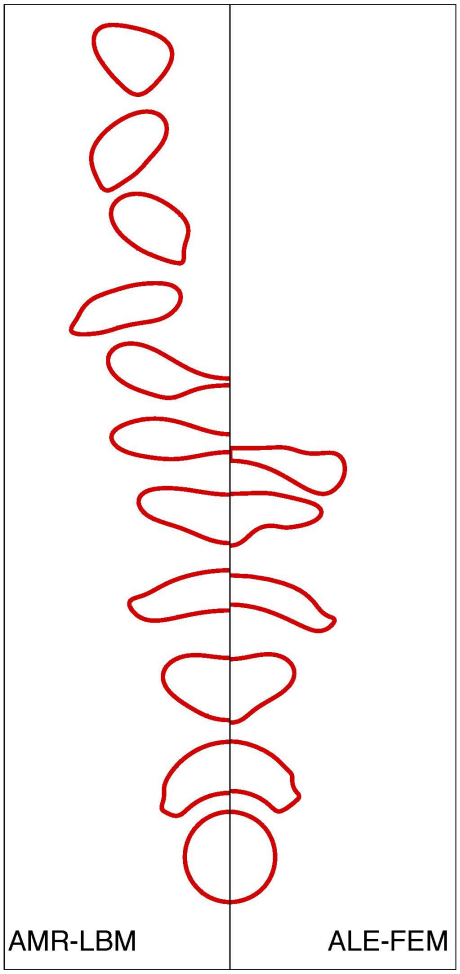

Figure 10: Time evolution of the bubble shape, with comparison made at the same position, computed for $\mu_L = 2 \times 10^{-4}$ Pa·s and $\sigma = 0.001$ N/m such that Oh= 0.00633, Bo = 9.99 and $Re_g = 500$. Left: the AMR-LBM results. Right: the ALE-FEM results. Note that the ALE-FEM results are presented up to the point immediately before the breakup.

-3.75 mm) in the tube. The time evolution of the bubble velocity is plotted in figure 11(a) for ALE-FEM and AMR-LBM with different resolution. The resolution in the ALE-FEM simulations can be controlled by setting the number of nodes at the interface. For the red curves in figure 11, the number of interface nodes is 128. As a result, the resolution is about $\frac{1}{2}\pi D/128 : 2.5\text{mm} = \pi/640$, where 2.5 mm is the width of the computational domain. As to the resolution in the AMR-LBM simulations, the finest grid is $1/1024$ of the domain width 2.5 mm (black curves in figure 11). Note that in all the AMR-LBM simulations, the interfacial width W is always five times of the finest grid size, and hence it changes with the grid resolution. Figure 11(a) shows that the bubble accelerates immediately after its release. The velocity drops sharply toward zero when the bubble finally approaches the top wall. High frequency sub-oscillations [18] are observed in the "approach-bounce" cycles, which can be clearly observed from the ALE-FEM results (red curves) and the AMR-LBM results (black curves).

Figure 11(b) shows the time evolution of the aspect ratio, with the colors having the same correspondence as in figure 11(a). The bubble is circular in the beginning (with $A_R = 1$), and then it is immediately squashed (with $A_R > 1$) as its rising is accelerated. Besides the velocity sub-oscillations observed in figure 11(a), the aspect ratio displays sub-oscillations as well. In figures 11(a) and 11(b), it is readily seen that the higher resolution of LBM leads to results closer to the ALE-FEM ones.

In comparison to ALE-FEM results, the AMR-LBM results in subsection 3.3 are considered quantitative, and those in subsection 3.4 are considered semi-quantitative. Figure 11 shows the mesh convergence: the AMR-LBM results converge to the ALE-FEM results as the resolution is enhanced. Note that the interfacial width W is always five times of the finest grid size. Generally speaking, the difference between the AMR-LBM and ALE-FEM results decreases with the decreasing interfacial width. Hence, AMR-LBM can do a better job at a higher resolution, which demands a higher computational cost. To obtain reliable results in AMR-LBM computations, we need to choose good values for M and W, and a high resolution that we can afford. It will be more accurate if smaller values are used for the interfacial width W. However, there is a limit to do so: numerical instability would appear if W is made too small. As to the mobility M, lower values are desired. If M is too large, then there will be excessive numerical

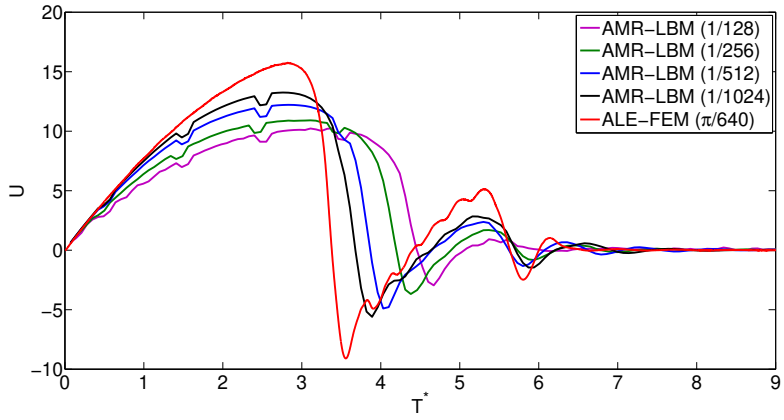

(a)

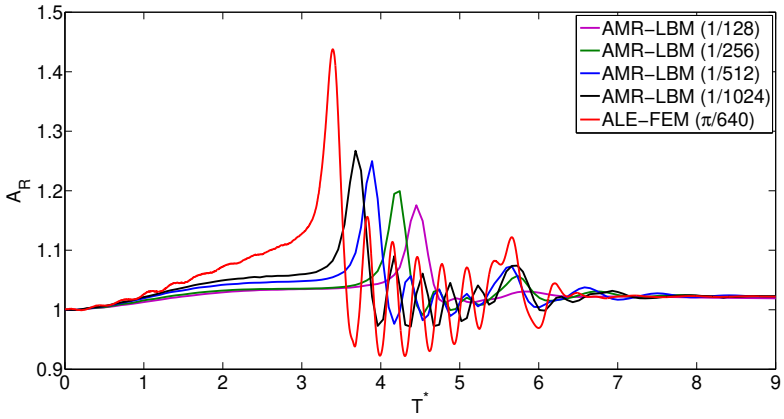

(b)

Figure 11: Comparison among the one ALE-FEM and four AMR-LBM simulations with different resolution (grid size), for a rising bubble with $\mu_L = 0.001$ Pa·s and $\sigma = 0.08$ N/m. (a) Time evolution of the bubble velocity. (b) Time evolution of the aspect ratio of the bubble.

dissipation leading to inaccurate results.

Figure 12 is for a further comparison between the two methods. The left half shows a series of snapshots taken in the AMR-LBM simulation with the $1/1024$ resolution (corresponding to the black curves in figure 11). The right half shows a series of snapshots taken in the ALE-FEM simulation with the $\pi/640$ resolution (corresponding to the red curves in figure 11). It is observed from figure 11 that the ALE-FEM simulation produces a bubble moving faster than that produced by the AMR-LBM simulations. In figure 12, the bubble rises first (upper left), approaches the wall and squeezes out the liquid between the bubble and the wall (upper right), arrives at a position closest to the wall (lower left), and bounces from the wall (lower right). The difference between the bubble shapes from the two methods can be clearly seen. In the lower right snapshots, the AMR-LBM results show a bounced bubble whose center is the farthest from the wall, and the ALE-FEM results show a bounced bubble that is still moving away from the wall.

Regarding the thin liquid film between the bubble and the wall, the ALE-FEM can accurately simulate its hydrodynamics [18]. When the AMR-LBM is used, the thin film hydrodynamics can be simulated with the help of continuous mesh refinement, which may be very expensive. This is simply caused by the diffuse interface which possesses a finite thickness that must be much smaller than the liquid film thickness and has to be resolved. As seen from the simulations for rising and bounced bubbles, the AMR-LBM results always show stronger damping than the corresponding ALE-FEM results, as seen in figures 11(a) and 11(b). This is caused by the diffusive transport which is inherent in the AMR-LBM but absent in the ALE-FEM.

4.3. On the efficiency

Comparison between the performances of the ALE-FEM and AMR-LBM for the rising and bounced bubbles in Sec. 4.2 is made in table 1. Our simulations are carried out on an Intel(R) Core(TM) workstation with CPU i7−4770 @3.40GHz and 12GB RAM. The GNU FORTRAN is used to carry out all the AMR-LBM simulations and GNU C is used to carry out all the ALE-FEM simulations.

The data in table 1 cover the dimensionless time period from $T^* = 0$ to 9 for the

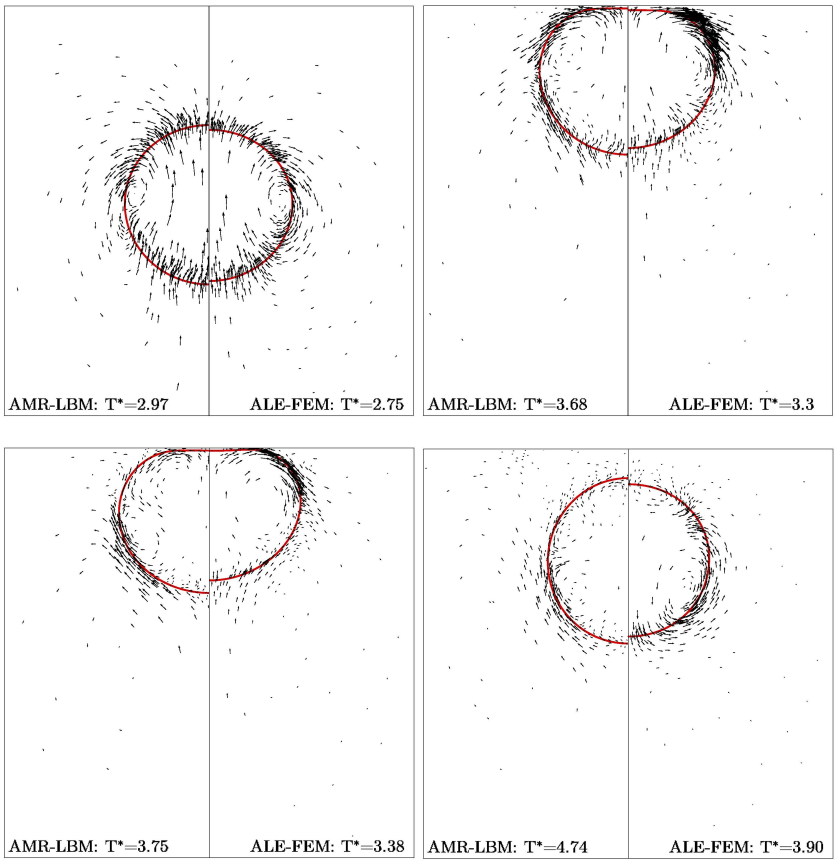

Figure 12: Snapshots showing the bubble shape and velocity field, obtained from the AMR-LBM with the $1/1024$ resolution and the ALE-FEM with the $\pi/640$ resolution. They correspond to the black and red curves in figure 11.

bubbles simulated in Sec. 4.2. The time step ΔT^* corresponds to the resolution which can ensure the stability of the program. The AMR-LBM code is parallelized by using OpenMP to speed up the simulations. The ALE-FEM code is difficult to parallelize. We use 4 cores for all the simulations by AMR-LBM and only 1 core for ALE-FEM simulations. The AMR-LBM with the $1/512$ resolution is faster than the ALE-FEM with the $\pi/640$ resolution by more than 10 times. However, as the resolution of AMR-LBM increases, the CPU time grows very fast. As a result of the parallelizability, the AMR-LBM possesses better computational efficiency. But the high resolution demanded by

Method	Finest mesh [of 2.5 mm]	ΔT^*	Cores used	CPU time [sec]
AMR-LBM	$1/128$	4.4×10^{-5}	4	379.1
AMR-LBM	$1/256$	3.1×10^{-5}	4	844.8
AMR-LBM	$1/512$	7.7×10^{-6}	4	6759.8
AMR-LBM	$1/1024$	1.9×10^{-6}	4	63535
ALE- FEM	$\pi/640$	2.5×10^{-5} (initial value) 3.13×10^{-6} (final value) 1.4×10^{-5} (average value)	1	329163

Table 1: Finest mesh, time step ΔT^*, number of cores used, and CPU run time for the five simulations used in Fig. 11. The time step (initial, final and average) in ALE-FEM is listed here because it is adaptive in order to meet the CFL condition.

the accurate simulations turns out to be very expensive. These make the AMR-LBM a reasonably good and very efficient numerical tool, although its quantitative predictions are not entirely reliable.

5. Conclusions

In this work, the dynamics of a bubble in a surrounding liquid has been numerically investigated in two dimensions using the AMR-LBM and ALE-FEM. The numerical results from the two methods have been compared for three different situations. We start from a validation study in which a static bubble is used to test the two methods. The spurious velocities are found to be negligibly small at numerical equilibrium. We then turn to the oscillatory behaviors of suspended bubbles in the absence of gravity. The numerical results from the two methods are in quantitative agreement. We finally investigate the oscillatory behaviors of rising bubbles in the presence of gravity. The numerical results from the two methods are in semi-quantitative agreement for all the cases. The AMR-LBM results show a stronger damping effect due to the diffusive transport inherent in the diffuse interface modeling. Our investigation of the oscillatory behaviors focuses on the underdamped and overdamped dynamics observed from the bubble shape and velocity (for rising bubbles). The transition between these two regimes is controlled by the dimensionless parameter Oh, which is varied by varying either the liquid viscosity or the surface tension. As Oh increases from a sufficiently

small value, the bubble dynamics displays a transition from the underdamped to the overdamped regime, with a critical Oh $\simeq 0.1$. Finally, we want to point out that accurate simulations for interfacial dynamics have been a classic topic for decades. In fact, each of the two methods reported here still has space for improvement, and the comparative study can be further carried out for more complicated examples and in three dimensions [19, 20]. Work in this direction is currently underway.

Acknowledgments

CJZ and LSL would like to acknowledge the support from CSRC through NSFC Grant U1530401. CJZ and TZQ would like acknowledge the support from Hong Kong RGC through the Collaborative Research Fund under the grants C6004-14G and C1018-17G.

References

[1] M. Van Dyke, An Album of Fluid Motion, Parabolic, Palo Alto, CA, 1984.

[2] M. Samimy, K. S. Breuer, L. G. Leal, P. H. Steen, A Gallery of Fluid Motion, Cambridge University Press, Cambridge, UK, 2004.

[3] P. C. Duineveld, The rise velocity and shape of bubbles in pure water at high Reynolds number, Journal of Fluid Mechanics 292 (1995) 325.

[4] R. Clift, J. Grace, M. Weber, Bubbles, Drops, and Particles, Dover Civil and Mechanical Engineering Series, Dover, Mileola, New York, 2005.

[5] A. Albadawi, D. Donoghue, A. Robinson, D. Murray, Y. Delauré, On the assessment of a VOF based compressive interface capturing scheme for the analysis of bubble impact on and bounce from a flat horizontal surface, International Journal of Multiphase Flow 65 (2014) 82–97.

[6] D. Kosior, J. Zawala, K. Malysa, Influence of n-octanol on the bubble impact velocity, bouncing and the three phase contact formation at hydrophobic solid

surfaces, Colloids and Surfaces A: Physicochemical and Engineering Aspects 441 (2014) 788–795.

[7] S. Popinet, S. Zaleski, Bubble collapse near a solid boundary: a numerical study of the influence of viscosity, Journal of Fluid Mechanics 464 (2002) 137–163.

[8] T. Qin, S. Ragab, P. Yue, Axisymmetric simulation of the interaction of a rising bubble with a rigid surface in viscous flow, International Journal of Multiphase Flow 52 (2013) 60–70.

[9] I. Seric, S. Afkhami, L. Kondic, Direct numerical simulation of variable surface tension flows using a Volume-of-Fluid method, Journal of Computational Physics 352 (2018) 615–636.

[10] J. Étienne, E. J. Hinch, J. Li, A Lagrangian-Eulerian approach for the numerical simulation of free-surface flow of a viscoelastic material, Journal of Non-Newtonian Fluid Mechanics 136 (2006) 157–166.

[11] J. Li, An arbitrary Lagrangian Eulerian method for three-phase flows with triple junction points, Journal of Computational Physics 251 (2013) 1–16.

[12] A. Fakhari, M. Geier, T. Lee, A mass-conserving lattice Boltzmann method with dynamic grid refinement for immiscible two-phase flows, Journal of Computational Physics 315 (2016) 434–457.

[13] X. He, L.-S. Luo, Theory of the lattice Boltzmann method: From the Boltzmann equation to the lattice Boltzmann equation, Physical Review E 56 (1997) 6811–6817.

[14] A. Fakhari, T. Lee, Multiple-relaxation-time lattice Boltzmann method for immiscible fluids at high Reynolds numbers, Physical Review E 87 (2013) 023304.

[15] A. Fakhari, D. Bolster, L.-S. Luo, A weighted multiple-relaxation-time lattice Boltzmann method for multiphase flows and its application to partial coalescence cascades, Journal of Computational Physics 341 (2017) 22–43.

[16] D. Jacqmin, Contact-line dynamics of a diffuse fluid interface, Journal of Fluid Mechanics 402 (2000) 57–88.

[17] T. Zhang, B. Shi, Z. Guo, Z. Chai, J. Lu, General bounce-back scheme for concentration boundary condition in the lattice-Boltzmann method, Physical Review E 85 (2012) 016701.

[18] C. Zhang, J. Li, L.-S. Luo, T. Qian, Numerical simulation for a rising bubble interacting with a solid wall: Impact, bounce, and thin film dynamics, Physics of Fluids 30 (2018) 112106.

[19] K. Sankaranarayanan, I. Kevrekidis, S. Sundaresan, J. Lu, G. Tryggvason, A comparative study of lattice Boltzmann and front-tracking finite-difference methods for bubble simulations, International Journal of Multiphase Flow 29 (2003) 109–116.

[20] S. Mukherjee, A. Zarghami, C. Haringa, K. van As, S. Kenjereš, H. E. V. den Akker, Simulating liquid droplets: A quantitative assessment of lattice Boltzmann and volume of fluid methods, International Journal of Heat and Fluid Flow 70 (2018) 59–78.